Graphical Direct Writing of Macroscale Domain Structures with Nanoscale Spatial Resolution in Nonpolar-Cut Lithium Niobate on Insulators

Yuezhao Qian, Ziqing Zhang, Yuezhou Liu, Jingjun Xu, and Guoquan Zhang ⓘ*

The MOE Key Laboratory of Weak-Light Nonlinear Photonics, School of Physics and TEDA Applied Physics Institute, Nankai University, Tianjin 300457, China

We report on a graphical domain engineering technique with the capability to fabricate macroscale domain structures with nanoscale spatial resolution in nonpolar-cut lithium-niobate thin film on insulators through the biased probe tip of scanning atomic force microscopy. It is found that the domain writing process is asymmetric with respect to the spontaneous polarization $\mathbf{P}_s$ even though the tip-induced poling field is mirror symmetric. Various domain structures, with a dimension larger than millimeters while consisting of nanoscale domain elements and with arbitrary domain-wall inclination angle with respect to $\mathbf{P}_s$, are designed graphically and then written directly into nonpolar-cut lithium-niobate crystals. As a proof-of-principle demonstration, periodically poled *x*-cut lithium-niobate thin film on insulators with a period of 600 nm, a depth of 460 nm, and a length of approximately 1 mm is fabricated. This technique could be useful for device applications in integrated optics and optoelectronics and domain-wall nanoelectronics based on lithium niobate on insulators.

I. INTRODUCTION

Lithium-niobate (LN) crystal is of excellent electro-optic, pyroelectric, piezoelectric, acousto-optic, and nonlinear optical properties, especially with the maturation of the fabrication technique of lithium niobate on insulators (LNOI) [1–5], providing a golden material platform for various ferroelectric, optoelectronic, and nonlinear optical applications such as ferroelectric and holographic memories [6–8], electro-optic modulator [9–11], optical waveguide, and integrated optics [4,12], and nonlinear optical frequency conversion [13–17], to just mention a few. The ferroelectric LN crystal is of 180° domain structure, and its ferroelectric domain can be inverted and designed to improve the device performance, for example, the nonlinear optical frequency conversion efficiency can be improved through periodically poled LN (PPLN) based on the quasi-phase-matching technique [18,19]. Various domain-poling techniques were developed, including the traditional electric-field-poling technique [20,21], the light-assisted domain inversion technique [22], the direct laser pulse and electron beam irradiation techniques [23–26], and the tip-field-induced domain-inversion technique via a scanning probe microscope [27–33]. Currently, PPLN with a domain period in micrometers can be easily fabricated in both *z*-cut and nonpolar-cut (*x*-cut or *y*-cut) LN crystals. Nanoscale domain structures were also reported in *z*-cut bulk LN or LNOI, while most of them

in bulk LN are surface structures with their size limited by the lateral domain expansion effect during the domain growth [29,34]. Therefore, up to now, it is still a challenging task to produce PPLN with a submicron period in nonpolar-cut LN crystals, which is usually required to achieve the parametric interaction of counterpropagating light beams based on the quasi-phase-matching technique and to use the largest nonlinear coefficient d_{33} of LN crystal with improved nonlinear optical frequency conversion efficiency [35,36]. Tremendous efforts have been made and several groups have tried to fabricate PPLN with submicron periodicity in nonpolar-cut LN by employing the in-plane electric-field-poling technique with a finger-poling electrode configuration, however, the quality of the submicron PPLN still cannot meet the requirement of practical applications such as nonlinear frequency conversion [15,37–40].

More recently, the domain wall of LN was found to be conductive, which makes it also possible for applications in nanoelectronics [41,42]. The domain-wall conductivity in LN is proportional to $2P_s \sin\theta$, where $\mathbf{P}_s$ is the spontaneous polarization of LN and θ is the inclination angle of the domain wall with respect to $\mathbf{P}_s$ [43]. Unfortunately, the domain-wall inclination angle θ was found to be almost impossible to control precisely and was small and less than approximately 5° in *z*-cut LN crystals, which puts a serious limitation on the optimization of domain-wall conductivity in LN [44–47]. Therefore, it is desired to develop a method to fabricate domain walls with large inclination angle θ in a precisely controllable way.

*zhanggq@nankai.edu.cn

In this paper, we report on the successful fabrication of high-quality PPLN with a submicron periodicity and a longitudinal length longer than millimeters in nonpolar-cut LNOI by scanning the biased probe tip of an atomic force microscope (AFM). Domain structures with arbitrary shape and domain-wall inclination angle, and with the size ranging from tens of nanometers to millimeters or longer, are predesignable in a graphical way and can then be written directly into nonpolar-cut LNOI through the biased AFM tip. This technique is useful in the precise design of domain structures in LNOI for practical applications in nanoelectronics, integrated optics, nonlinear optical frequency conversion, and parametric interaction of counter-propagating beams with high efficiency.

II. EXPERIMENTAL RESULTS

Figure 1(a) shows the schematic diagram to fabricate the domain structures in nonpolar-cut LNOI with a positively biased AFM tip. In the experiments, we use a x-cut LNOI sample consisting of a 600-nm Mg-doped (5.0 mol.%) x-cut LN thin film, a 2-μm silica, and a 500-μm LN substrate bonded to each other in sequence. The spontaneous polarization $\mathbf{P}_s$ of the x-cut LN thin film is in the surface plane of the x-cut LN and is set to be along the z-axis of the experimental coordinate system, as shown in Fig. 1(a). The AFM tip with a radius of 30 nm is in contact with the top surface
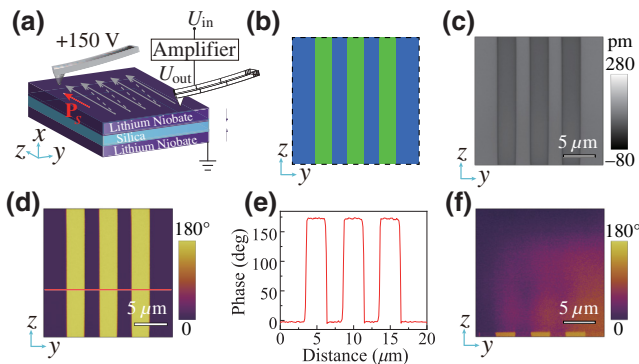

FIG. 1. (a) Schematic diagram to fabricate domain structures in x-cut LNOI by scanning the positively biased AFM tip along the spontaneous polarization $\mathbf{P}_s$, the gray arrows indicate the scanning direction of the AFM tip. (b) The graphical map used to produce domain stripes, where a positive voltage is applied on the scanning AFM tip in the green regions while no voltage is applied on the AFM tip in the blue regions. (c) The PFM amplitude image of the fabricated domain stripes. (d) The PFM phase image of the fabricated domain stripes. (e) The phase distribution profile of the fabricated domain stripes along the red solid line in (d). (f) The PFM phase image of the x-cut LNOI surface when the positively biased AFM tip is scanned antiparallel to the spontaneous polarization $\mathbf{P}_s$ based on the designed voltage map shown in (b).

of the x-cut LN thin film, and is loaded with a positive voltage and scanned in the direction parallel to the spontaneous polarization $\mathbf{P}_s$ of the x-cut LN according to a predesigned graphical map, for example, as that shown in Fig. 1(b), where the AFM tip is positively biased when scanning in the green regions, while the AFM tip is grounded when scanning in the blue regions. Typical domain stripes are fabricated in x-cut LNOI according to the graphical map shown in Fig. 1(b), in which the AFM tip voltage is 150 V when scanning in the green regions with a scanning speed of 80 μm/s. The domain stripes are characterized by using piezoresponse force microscopy (PFM, MFP-3D Infinity, Asylum Research, Goleta, CA, USA. The detailed measurement information can be found in Appendix A), and the PFM amplitude and phase images are shown in Figs. 1(c) and 1(d), respectively. Note that theoretically the PFM amplitude contrast for different domains with antiparallel orientations is the same. Here, the amplitude contrast and range for different domains with antiparallel orientations are different, most probably is due to the fact that the measurements are not completely decoupled from the cantilever dynamics and the electrostatic effect of the accumulated surface charges, which makes the PFM amplitude of one domain orientation always lower than that of the other [48–50]. Figure 1(e) is the phase distribution profile along the red solid line in Fig. 1(d). One sees that the graphical map in Fig. 1(b) is exactly mapped into the domain stripes in x-cut LNOI. However, we find that the domain stripes cannot be written into the x-cut LNOI when the AFM tip is scanning in the direction antiparallel to the spontaneous polarization $\mathbf{P}_s$, and only the small area just in front of the scanning tip at the scanning tail terminal is found to be inverted, as shown in Fig. 1(f).

Surprisingly, the domain stripes can be written into the x-cut LNOI when the AFM tip is scanning in the direction antiparallel to the spontaneous polarization $\mathbf{P}_s$ but applied with a negative voltage, as shown in Fig. 2(a). The predesigned graphical map is shown in Fig. 2(b), in which the AFM tip is applied with a negative voltage when scanning in the orange regions, while it is grounded when scanning in the blue regions. Figures 2(c) and 2(d) show the PFM amplitude and phase images of the fabricated domain stripes when the AFM tip is applied with a negative voltage of −150 V and scanning with a speed of 80 μm/s according to the graphical map in Fig. 2(b). The PFM phase distribution profile of the domain stripes along the red solid line in Fig. 2(d) is shown in Fig. 2(e). Again, one sees that the graphical map in Fig. 2(b) is exactly mapped into the domain stripes in x-cut LNOI. Note that, in contrast to the case with a positively biased AFM tip, in this case the domain stripes cannot be written into the x-cut LNOI when the negatively biased AFM tip is scanning in the direction parallel to the spontaneous polarization $\mathbf{P}_s$, and only a small part of the domain stripes are written into the x-cut LNOI at the areas just in front of the scanning AFM
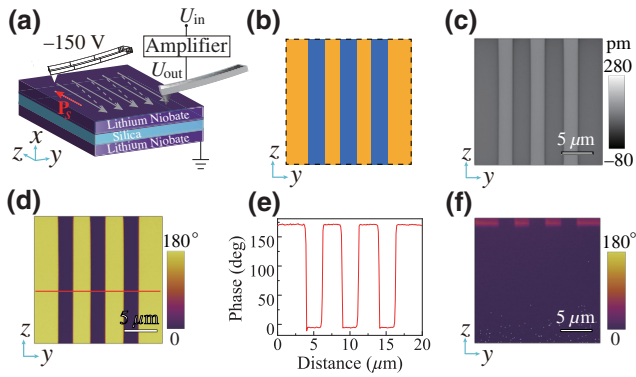
FIG. 2. (a) Schematic diagram to fabricate domain structures in x-cut LNOI by scanning the negatively biased AFM tip antiparallel to the spontaneous polarization $\mathbf{P}_s$, the gray arrows indicate the scanning direction of the AFM tip. (b) The graphical map used to produce the domain stripes, where a negative voltage is applied on the scanning AFM tip in the orange regions while no voltage is applied on the AFM tip in the blue regions. (c) The PFM amplitude image of the fabricated domain stripes. (d) The PFM phase image of the fabricated domain stripes. (e) The phase distribution profile of the fabricated domain stripes along the red solid line in (d). (f) The PFM phase image of the x-cut LNOI surface when the negatively biased AFM tip is scanned parallel to the spontaneous polarization $\mathbf{P}_s$ based on the designed graphical voltage map shown in (b).

FIG. 3. (a) PFM phase image of the domain stripes fabricated in the x-cut LNOI with a rectangular trench etched by using FIB after a 3-h HF-acid etching. The red and white arrows represent the polarization direction of the respective domain stripes. (b) The AFM height map of the trench after a 3-h HF-acid etching, the red and blue vertical lines indicate the location of the $+z$ and $-z$ face of the domain stripes, respectively. (c) The magnified AFM height map of the $-z$ face of the central domain stripe in (b). (d) The height profile across the etched $-z$ face of the domain stripe along the white line in (c), the depth of the inverted domain stripe is measured to be 460 nm.

tip at the scanning tail terminal, as shown in Fig. 2(f). We give a detailed explanation on the anisotropic behavior of the graphical direct-domain writing through a biased AFM tip in Sec. III. Note that the domain structures graphically written by the biased AFM tip are stable, and no noticeable degradation is observed after an on-shelf time interval of one year, as shown in Appendix C. Similar to the case in z-cut LN crystal, the bounded charges associated with the change of the electric dipole moment in x-cut LN crystal are compensated by the injected charges through the biased AFM tip, the bulk-free charges (electrons or holes for the head-to-head or tail-to-tail domain walls, which make the domain walls conductive) and the compensating surface charges from the surrounding environment. The inverted domains are stable due to the balance among the internal field, the screening field induced by various screening charges, and the depolarization field.

To measure the depth of the inverted domain stripes, one first fabricates the domain stripes by scanning the negatively biased AFM tip in the direction antiparallel to the spontaneous polarization $\mathbf{P}_s$ with a -150-V voltage and a scanning speed of 80 μm/s. Then we produce a rectangular trench with a depth of 600 nm across the domain stripes by employing focused ion-beam (FIB) etching, so that the $+z$ face and $-z$ face of the domain stripes are exposed to air. The sample is then immersed in the HF acid with a concentration of 42% for 3 h, and the $-z$ face of the domain stripes is etched much faster than the $+z$ face
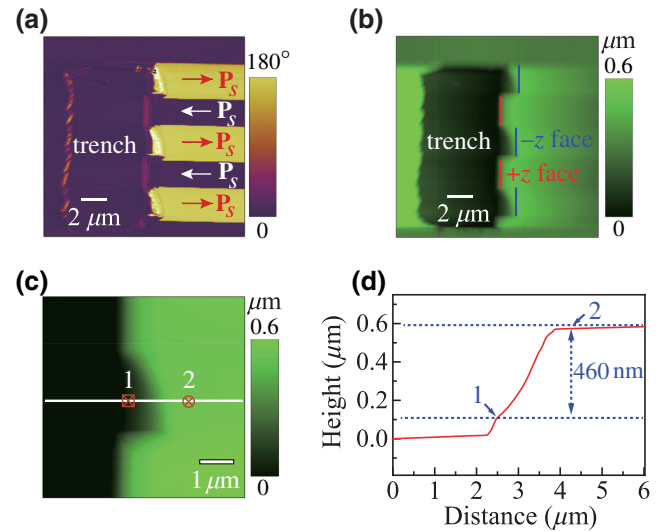
because of the selective etching property of the LN crystals. The HF-acid etching rate of the $-z$ face of Mg-doped LN (5.0 mol.%) is measured to be 0.53 μm per hour with a HF acid concentration of 42% (see Appendix B), while the $+z$ face of LN is almost not etched. The PFM phase image and the AFM height map of the etched domain structures are shown in Figs. 3(a) and 3(b). Figure 3(c) shows the magnified AFM height map around the $-z$ face of the central domain stripe in Fig. 3(b), and the height profile of the domain structure along the white line in Fig. 3(c), which is across the etched $-z$ face of the central domain stripe, is shown in Fig. 3(d), from which the depth of the inverted domain stripe is measured to be approximately 460 nm. Note that the depth of the inverted domain is dependent on the dopant and the Li/Nb ratio of LN because the coercive field is different for LN with different dopants and Li/Nb ratios, for example, the coercive field of the nominally pure congruent LN is 21 kV/mm, much higher than that of Mg-doped LN, and the depth of the inverted domain in nominally pure congruent LN, written by a 150-V biased AFM tip scanning in the direction parallel to the spontaneous polarization $\mathbf{P}_s$ at a speed of 80 μm/s is measured to be approximately 133 nm.

One notes that the etched $-z$ face of the trench is oblique, as shown in Fig. 3(d). In our case, the $-z$ face exposed to the HF-acid solution is the side wall of a trench

with a volume of tens of μm^3, and the HF-acid solution in the trench cannot be refreshed timely, especially at the bottom of the trench, therefore the HF-acid concentration in the trench will become lower and lower because the etching reaction consumes the HF acid but cannot be refreshed timely, while on the top surface the HF-acid solution can be refreshed timely and the HF-acid concentration on the top surface is relatively higher than that at the bottom of the trench, resulting in a HF-acid concentration gradient along the depth of the trench during the etching process. Note that the etching rate is larger at a higher HF-acid concentration, therefore, the etched $-z$ face of the trench shows an oblique side wall. Note that the length of etched LN on the top surface is around 1.5 μm, as shown in Fig. 3(d), in good agreement with the measured etching rate of the $-z$ face of Mg-doped LN.

In addition, the SiO_2 underneath the LN thin film will also be exposed to the HF-acid solution, and the SiO_2 will be etched quickly once it is exposed to the HF-acid solution, therefore, the LN thin film can be peeled off finally. Here, to avoid the LN thin film being peeled off from the substrate, we smear a thin layer of paraffin on the outside face of the LNOI sample, so that the LN thin film will not be peeled off even when the underneath SiO_2 is totally etched, and finally the LN thin film will adsorb on the surface of the 500-μm LN substrate directly. From Fig. 3(d), it can also be verified that the thickness of LN thin film of LNOI is 600 nm, in good agreement with that claimed by the company.

III. DISCUSSIONS

One notes that the domain structures can be directly written into the x-cut LNOI when the positively biased AFM tip scans in the direction parallel to $\mathbf{P}_s$, or the negatively biased AFM tip scans in the direction antiparallel to $\mathbf{P}_s$, but not vice versa. The reason is that the lateral in-plane component of the electric field generated by the biased AFM tip is of opposite direction on the two lobe sides of the AFM tip. Figure 4 shows the numerically simulated distribution of the lateral in-plane parallel component of the electric field generated by the biased AFM tip, in which the lateral in-plane parallel electric field component E_z is the electric field component parallel to $\mathbf{P}_s$ in the $x - z$ or $y - z$ planes. In the simulation, the relative dielectric constant of LN is $\epsilon_{11} = 44$ and $\epsilon_{33} = 29$, respectively. The radius of the AFM tip is set to be 30 nm, and the tip is in direct contact with the top surface of the x-cut LNOI. The biased voltage is 150 V for Figs. 4(a) and 4(c), and is -150 V for Figs. 4(b) and 4(d), respectively. The red thin curves in Fig. 4 show the location where E_z is equal to 4.5 kV/mm, i.e., the contour curves of the coercive field of Mg-doped LN [20]. One sees that the electric field component E_z is strong enough to invert the domain polarization around the biased AFM tip, and the depth of the inverted domain can
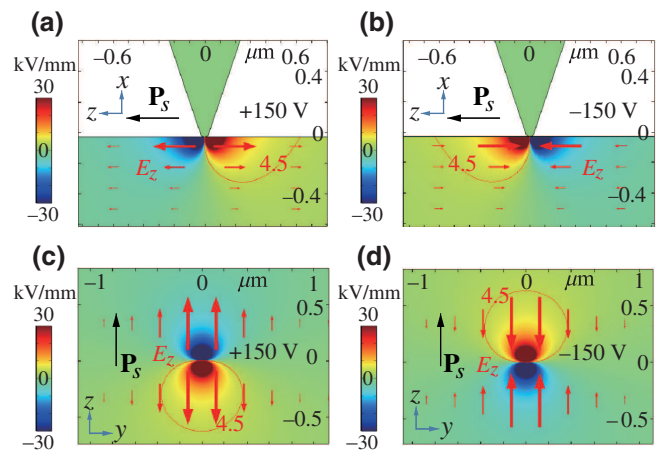

FIG. 4. (a),(c) Spatial distribution of E_z in the $x - z$ and $y - z$ planes, respectively, produced by the positively biased AFM tip with a 150-V voltage. (b),(d) Spatial distribution of E_z in the $x - z$ and $y - z$ planes, respectively, generated by the negatively biased AFM tip with a -150-V voltage. The red arrows represent the tip-induced electric field component E_z. The red solid thin curves in all figures are the contour curves of the coercive field with a value of 4.5 kV/mm for Mg-doped LN crystals.

be deeper than 300 nm determined by the contour curves of the coercive field. The experimentally measured depth of the domain stripes is slightly larger than the simulated one determined by the contour curves of the coercive field, this is due to the fact that the domain can grow even when the external electric field is lower than the coercive field, as also observed and confirmed by other groups in LN crystals [32,33].

One sees that the poling electric field E_z along the spontaneous polarization $\mathbf{P}_s$ is pointing towards the negatively biased AFM tip and/or pointing away from the positively biased AFM tip, this facilitates domain inversion when the biased AFM tip scans in the direction parallel to or antiparallel to the spontaneous polarization with positively or negatively biased AFM tip. Figure 5 shows the domain inversion with a stationary biased AFM tip and the asymmetric effect of the electric field induced by the biased AFM tip on the neighboring previously inverted domain, which provides further experimental evidence for the asymmetric domain-inversion behavior induced by the biased AFM tip. The domain inversion induced by the biased AFM tip is asymmetric in two aspects. First, the domain structure induced by a stationary biased AFM tip is asymmetric, resulting in a wedgelike domain with a stationary biased AFM tip. Second, the inverted wedgelike domain could be reserved or erased by the electric field generated by the neighboring biased AFM tip, depending on not only the polarity of the biased AFM tip but also the relative positions between the inverted wedgelike domain and the biased AFM tip. For instance, as shown in Fig. 5, one wrote a domain structure in the x-cut LNOI with the

biased AFM tip at point A, and then lifted the AFM tip and moved the AFM tip to the next point B, there one wrote another domain structure with the biased AFM tip. In this way, one wrote five domain structures in sequence with the biased AFM tip with different neighboring interval distance of 3 μm and 1 μm, respectively. One notes that a wedgelike domain structure is formed no matter whether the AFM tip is positively or negatively biased with a voltage magnitude larger than 65 V, and only the area on one side of the biased AFM tip with its domain polarization antiparallel to E_z is inverted, while the area on the opposite side of the biased AFM tip with its polarization parallel to E_z is kept to unchanged, as shown in Figs. 5(b1) and 5(e1). Similar tip-induced wedgelike domain structures were also observed by other groups in nonpolar-cut LN crystals [32,33]. Interestingly, the wedgelike domain structures are also dependent on the neighboring interval distance and the scanning direction of the biased AFM tip. For example, the wedgelike domain structures are well isolated from each other when the neighboring interval distance is large enough, irrespective of the polarity and the scanning direction of the biased AFM tip. On the other hand, when the neighboring interval distance is small enough, it is possible that the wedgelike domain structure written by the biased AFM tip could be partially or totally erased by the subsequently followed domain writing process, as shown in Figs. 5(b2), 5(b4), 5(e2) and 5(e4). This is because the formerly inverted domain polarization is switched back by the electric field induced by the subsequent neighboring biased AFM tip, for example, when the tip is moved from point B to point A in Fig. 5(c) or from point A to point B in Fig. 5(f), due to the fact that the directions of the tip-induced electric field component E_z on the two sides of the biased AFM tip are exactly opposite with respect to each other along the z axis, as shown in Fig. 4. Note that there are still some traces of partially inverted domains reminded in the central area of Fig. 1(f), indicating that the inverted domain is not completely flipped back to the original state. On the other hand, however, the wedgelike domain stripes written by the biased AFM tip in sequence can also be connected one after another and form a long continuous domain stripe, as shown in Figs. 5(b3) and 5(e3), when the positively biased AFM tip scanning in the direction parallel to $\mathbf{P}_s$ [see Fig. 5(a)] or the negatively biased AFM tip scanning in the direction antiparallel to $\mathbf{P}_s$ [see Fig. 5(d)] with a small enough neighboring interval distance. In this way, domain stripes as those shown in Figs. 1(d) and 2(d) can be directly written via the biased AFM tip.

The inverted domain can be reversed again by an appropriately biased AFM tip scanning in appropriate direction, therefore the inverted domain will flip back to the original state. This also means that the domain wall can be moved intentionally. Figure 6 shows the results of intentional domain reversion and domain-wall movement operation with a biased AFM tip. Here, one produces a square
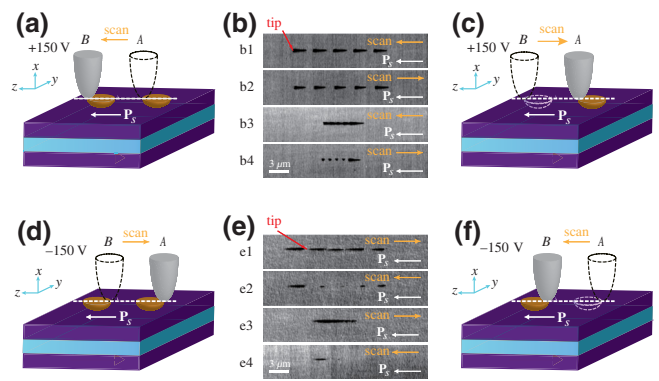

FIG. 5. (a),(c) Schematic diagrams to write the domain structures with a positively biased AFM tip scanning in different directions with respect to $\mathbf{P}_s$. (b) PFM amplitude images of the domain structures written with a +150-V biased AFM tip, wherein (b1),(b3) represent the cases that the tip scanned in the direction parallel to $\mathbf{P}_s$ but with different neighboring interval distance of 3 μm and 1 μm, respectively. (b2),(b4) show the cases with the tip scanning in the direction antiparallel to $\mathbf{P}_s$ but with different neighboring interval distance of 3 μm and 1 μm, respectively. (d),(f), Schematic diagrams to write domain structures with a negatively biased AFM tip scanning in different directions with respect to $\mathbf{P}_s$. (e) PFM amplitude images of the domain structures generated with a −150-V biased AFM tip, wherein (e1),(e3) represent the cases that the tip scanned in the direction antiparallel to $\mathbf{P}_s$ but with different neighboring interval distance of 3 μm and 1 μm, respectively. (e2),(e4) show the cases with the tip scanning in the direction parallel to $\mathbf{P}_s$ but with different neighboring interval distance of 3 μm and 1 μm, respectively.

inverted domain with a 150-V biased AFM tip scanning in the direction parallel to the spontaneous polarization $\mathbf{P}_s$ at a speed of 80 μm/s [Fig. 6(a)], then the polarization of the bottom part of the inverted domain in the green rectangular box is reversed by scanning a −150-V biased AFM tip in a direction antiparallel to the local spontaneous polarization $\mathbf{P}_s$ (indicated by the red arrows in the yellow area) at a speed of 80 μm/s, so that the head-to-head domain wall is moved upward to the middle of the figure, as shown in Fig. 6(b). Such domain reversion and domain-wall movement can be operated repeatedly.

We find that the quality of the domain structures is dependent on the scanning speed of the biased AFM tip. If the scanning speed of the biased tip is too slow, then the inverted domain will laterally expand and the domain-structure profile will deviate significantly from that of the designed graphic map. On the other hand, if the scanning speed is too fast, then the domain inversion may not be able to follow the biased tip, and the domain may only be partially inverted and the domain structure also deviates significantly from the designed graphic map. Figure 7 shows typical domain structures written by the AFM tip with a bias of 150 V at different scanning speed, in which Fig. 7(a) is the designed graphic map (periodic stripes
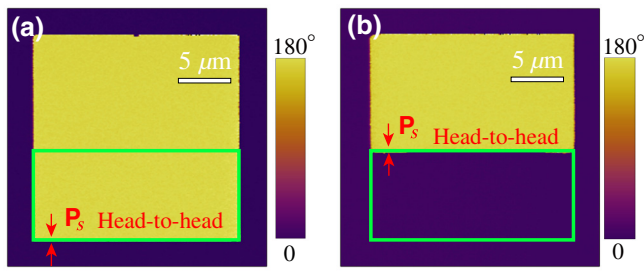
FIG. 6. (a) PFM phase image of a square inverted domain produced by a 150-V biased AFM tip scanning in a direction parallel to the local $\mathbf{P}_s$ at a scanning speed of 80 μm/s. (b) PFM phase image of a rectangular domain produced by reversing the bottom part of the square domain in the green rectangular box in (a) by scanning a -150-V biased AFM tip in the direction antiparallel to the local $\mathbf{P}_s$ at a speed of 80 μm/s.

with a period of 600 nm and a duty ratio of 0.5), and Figs. 7(b) and 7(c) show the domain structures written by the biased AFM tip at the scanning speed of 11.4 μm/s and 114 μm/s, respectively. One sees that the domain-structure profiles are deviated from that of the graphic map significantly in both cases. In practice, when the domain size is large enough, for example in the micrometer scale or larger, the domain-structure profiles written by the ± 150-V biased AFM tip are in good accordance with those of the graphic maps with a scanning speed of 80 μm/s, as shown in Figs. 1 and 2. Surely, when the domain size is small enough, for example, in the submicrometer range, a domain expansion of the order of tens of nanometers will induce noticeable deviation from the design graphic map. Therefore, one has to consider the domain expansion effect to fabricate the desired domain structures.

This graphical direct-writing technique is capable of graphically designing the domain structures and then mapping onto the nonpolar-cut LNOI via the biased AFM tip. Figure 8 shows various domain structures fabricated through this graphical direct-writing technique via the biased AFM tip in a 600-nm-thick *x*-cut LNOI, including PPLNs with domain period in submicron and micron scale [Figs. 8(a) and 8(b)], domain stripes with arbitrary domain-wall inclination angle θ [Fig. 8(c)], head-to-head
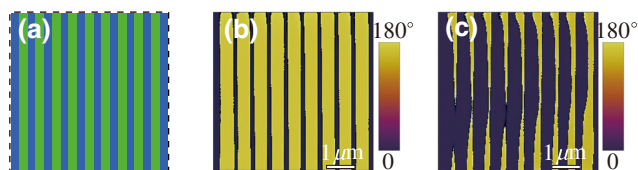

FIG. 7. (a) Designed graphical map with a period of 600 nm and a duty ratio of 0.5. (b) PFM image of the domain stripes written by a 150-V biased AFM tip with a scanning speed of 11.4 μm/s. (c) PFM image of the domain stripes written by a 150-V biased AFM tip with a scanning speed of 114 μm/s.
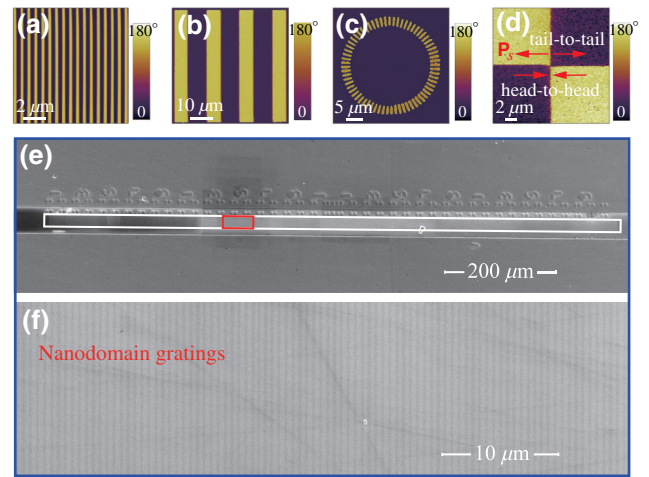

FIG. 8. Various domain structures fabricated in a 600-nm-thick Mg-doped (5.0 mol.%) *x*-cut LNOI via a -150-V biased AFM tip with a speed of 80 μm/s scanning in the direction antiparallel to the spontaneous polarization $\mathbf{P}_s$. (a) PFM phase image of PPLN with a grating period of 600 nm. (b) PFM image of PPLN with a grating period of 15 μm. (c) PFM image of domain stripes arranged on a circle with arbitrary domain-wall inclination angle θ. (d) PFM image of domain structures with head-to-head and tail-to-tail domain walls of a domain-wall inclination angle $\theta = 90°$. (e) SEM image of PPLN (in the white rectangular box) with a domain period of 600 nm and a longitudinal length of approximately 1 mm. (f) Magnified SEM image of nanodomain gratings of PPLN in the red rectangular box in (e).

and tail-to-tail domain walls with an inclination angle $\theta = 90°$ [Fig. 8(d)], and so on. The width of the domain stripes can be down to tens of nanometers (approximately 70 nm in our experiments). Figure 8(e) shows a PPLN with a domain grating period of 600 nm, a domain depth of approximately 460 nm, and a total longitudinal length of approximately 1 mm. Note that the scanning area of the AFM probe tip is limited within a scope of $90 \times 90 \ \mu$m^2. To fabricate domain structures long enough in the longitudinal dimension, we employ an overlay technique by dividing the whole area into separate divisions, each division with an area reachable by the AFM tip, and then mapping the domain structure into each division in sequence, as shown in Figs. 8(e) and 9. Figure 8(f) shows the magnified image of the nanodomain gratings in the red box of Fig. 8(e), which covers around two divisions, showing the good homogeneity of the fabricated submicron PPLN.

One may note that the key to get a good-quality PPLN is to achieve a seamless stitching of domain stripes in the neighboring divisions. Here, we first deposit a periodical array of Cr marker on the surface of LN with a period of 24 μm and a total length of approximately 1 mm (42 periods), as shown in Figs. 8(e) and 9, where each period of Cr marker corresponds to one division for domain stripe writing by using the biased AFM tip. Second, we find the
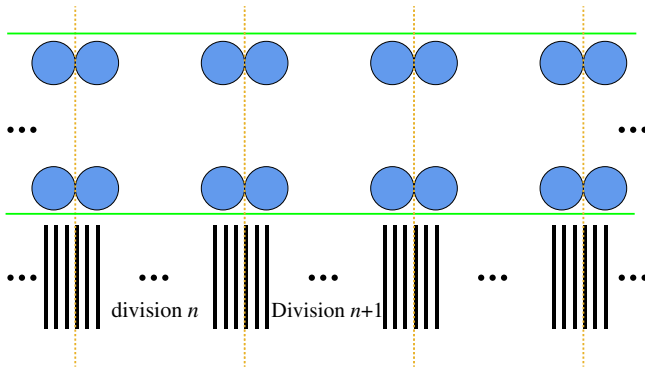
FIG. 9. Overlay scheme to fabricate macroscale domain structures with a nanoscale spatial resolution via a biased AFM tip of atomic force microscopy. The vertical orange dotted lines are the boundary between the neighboring divisions.
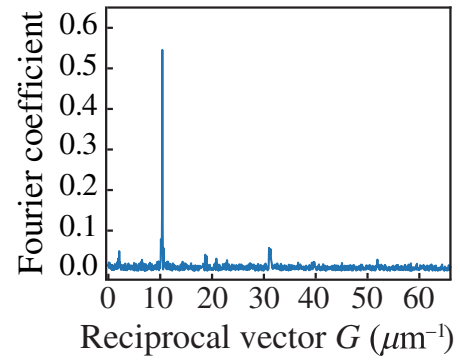

FIG. 10. Fourier transform of the fabricated PPLN composed of four stitched divisions in Fig. 8(e), showing a domain period of 600.38 nm and a duty ratio of 0.33, in good agreement with the designed one.

location of the first division according to the periodical Cr markers by measuring the AFM image around the first division, then we write 40 domain stripes into the first division with the biased AFM tip. Note that, considering the lateral domain expansion during the domain writing process, the duty ratio of the graphic stripe map is designed to be 0.2 to fabricate a PPLN with a duty ratio of 0.3. Here, to stitch the domain stripes in the first and the second divisions precisely, the key is to find precisely the location of the second division to write the periodical domain stripes. To achieve this seamless stitching of the periodical domain stripes in the two neighboring divisions, we measure the PFM images of the domain stripes in the first division with an area much larger than the first division ($60 \times 60 \ \mu m^2$ in the experiments), and then, according to the measured PFM image, we move *in situ* the AFM tip to the right place in the second division with an accuracy of approximately 15 nm, which is determined by the AFM system [51], where we write the periodical domain stripes in the second division. In this way, one can seamlessly stitch the periodical domain stripes in the neighboring divisions in sequence, therefore, to produce millimeter-long PPLN with a domain period of hundreds of nanometers. The time needed to find the location of the second division and write the periodical domain stripes in the second division is about 5 min, therefore, nearly 4 h are necessary to fabricate such a millimeter-long PPLN with the biased AFM tip.

To check the quality of the fabricated PPLN, we perform the Fourier transform of the written domain stripes composed of four stitched divisions in Fig. 8(e) and Fig. 9. The result is shown in Fig. 10, in which G is the reciprocal vector of the domain grating of the fabricated PPLN. One sees that, according to the Fourier spectrum, the period of the fabricated PPLN is verified to be 600.38 nm with a duty ratio of 0.33, in good agreement with the designed

one, indicating that the fabricated PPLN is of good quality. Such nonpolar-cut submicron PPLNs are essential for parametric interaction of counterpropagating light beams and nonlinear conversion generation of ultraviolet light with the feasibility to use the largest nonlinear coefficient d_{33} based on quasi-phase-matching technique.

In addition, we also measure the current-voltage (I-V) curves of the domain walls with different inclination angle θ, as shown in Fig. 11. Here the domain walls are fabricated by the 150-V biased AFM tip scanning in the direction parallel to the spontaneous polarization $\mathbf{P}_s$ at a speed of 80 $\mu m/s$. Figure 11(a) shows the schematic setup to measure the I-V of the domain wall, where two 300-nm-thick Cr electrodes are deposited on the top surface of x-cut LNOI, covering the domain wall with a gap distance of 3 μm. Figure 11(b) shows the measured I-V curves of the head-to-head domain walls with inclination angles of $15°$, $45°$, $75°$, and $90°$, respectively. One sees that the conductivity of the head-to-head domain wall increases with the increase of the domain-wall inclination angle θ, in good agreement with the theoretical prediction [43]. However, the measurement on the tail-to-tail domain walls is not successful because the conductivity of a single tail-to-tail domain wall is too small to be detected reliably. The capability to fabricate conductive domain walls with arbitrary domain-wall inclination angle in a controllable and designable way may pave the way for applications in domain-wall nanoelectronics based on LNOI [42].

IV. CONCLUSION

In summary, we demonstrate a graphical direct-writing technique of domain structures in nonpolar-cut LNOI with a biased AFM tip. We show the asymmetric behavior of this domain direct-writing technique, in which the domain can be directly written into the nonpolar-cut LNOI when scanning the positively biased AFM tip in the direction parallel to $\mathbf{P}_s$ or scanning the negatively biased AFM tip
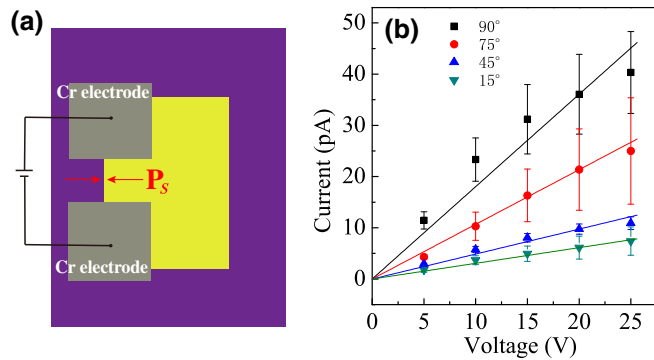
FIG. 11.   (a) Schematic diagram of the experimental setup to measure the *I*-*V* curves of the domain walls. (b) The measured *I*-*V* curves of the head-to-head domain walls with different inclination angles of $\theta = 15°, 45°, 75°,$ and $90°$, respectively.

in the direction antiparallel to **P**$_s$, but not vice versa. The tip voltage can be as low as 65 V. The depth of the inverted domain increases with the increase of the biased voltage, and it reaches approximately 460 nm with a biased voltage of 150 V and a scanning speed of 80 μm/s. Various domain structures, with the size ranging from nanoscale to millimeter-scale and with precisely controllable domain-wall inclination angle, are designed graphically and then mapped precisely into the nonpolar-cut LNOI. As a proof-of-principle demonstration, PPLN with a domain period of 600 nm, a domain depth of 460 nm, and a longitudinal length of approximately 1 mm is fabricated in a *x*-cut, Mg-doped (5.0 mol%) LNOI, which shows the possibility to use the largest nonlinear coefficient d_{33} in the nonlinear frequency conversion and parametric interaction of counterpropagating light beams based on the quasi-phase-matching technique. In addition, domain structures with head-to-head and tail-to-tail domain walls are also fabricated in the same LNOI sample. The capability to fabricate various domain structures with a nanoscale spatial resolution in a designable and controllable way makes this technique useful for device applications in integrated optics and optoelectronics and domain-wall nanoelectronics.

APPENDIX A: PFM MEASUREMENT

The PFM images are measured in the lateral mode through the cantilever torsion with a driving voltage of 5 V and a resonant frequency of 800 kHz, Ti/Ir-coated Si cantilevers with a force constant of 2.8 N/m and a probe tip radius of 30 nm are used. The instrument is MFP-3D Infinity from Asylum Research, Goleta, CA, USA.

APPENDIX B: MEASUREMENT ON THE ETCHING RATE OF THE $-z$ FACE OF MG-DOPED LN

It is verified experimentally that the etching rate of the LN surface in the HF-acid solution is anisotropic, and the $-z$ face of LN can be etched in HF-acid solution, while the $+z$ face is almost not etched. Figure 12 shows the measured time dependence of the etching depth of the $-z$ face of Mg-doped LN (5.0 mol.%) immersed in a HF-acid solution with a HF-acid concentration of 42%, from which a HF-acid etching rate of approximately 0.53 μm per hour can be obtained.

APPENDIX C: DEGRADATION TEST OF THE WRITTEN DOMAIN STRUCTURES

The domain structures written by the biased AFM tip are stable. Figures 13(a) and 13(b) show the PFM phase images of the domain stripes written by a positively $+150$-V biased tip scanning in the direction parallel to the spontaneous polarization **P**$_s$ measured with an on-shelf time gap of one year, and Fig. 13(c) shows the Fourier transform of the domain stripes, in which the upper part and the lower
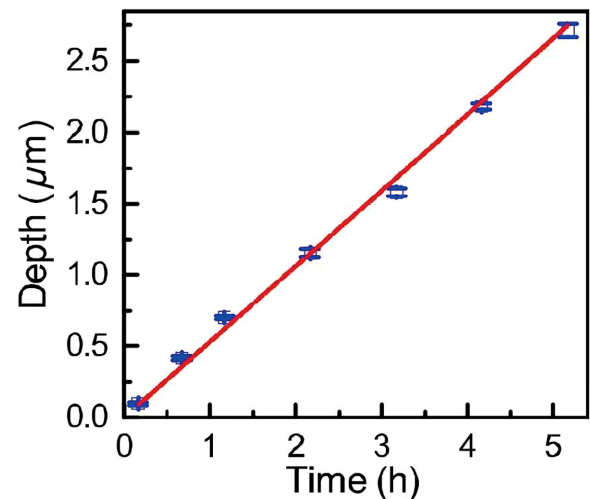

FIG. 12.   Measurement on the etching rate of $-z$ face of LN in the HF-acid solution with a HF-acid concentration of 42%. The crystal used is a Mg-doped LN with a Mg-doping concentration of 5.0 mol.%. The etching rate is measured to be approximately 0.53 μm per hour.
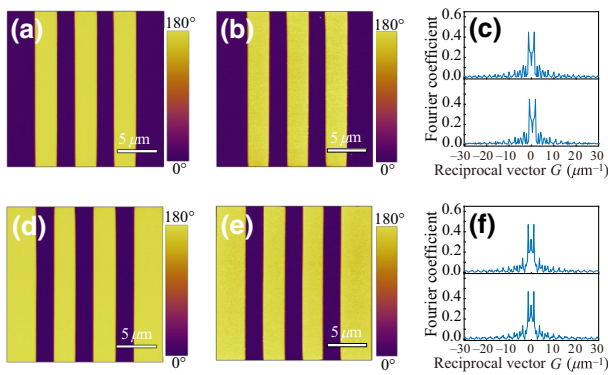
FIG. 13. (a),(b) PFM phase images of the domain stripes written by a positively +150-V biased tip scanning in the direction parallel to the spontaneous polarization $\mathbf{P}_s$ measured with an on-shelf time gap of one year. (c) Fourier transforms (upper part and lower part) of the fabricated domain stripes in (a),(b), respectively. (d),(e) PFM phase images of the domain stripes written by a negatively −150-V biased tip scanning in the direction antiparallel to the spontaneous polarization $\mathbf{P}_s$ measured with an on-shelf time gap of one year. (f) Fourier transforms (upper part and lower part) of the fabricated domain stripes in (d),(e), respectively. The tip scanning speed is 80 μm/s.

part correspond to the Fourier transform of the domain stripes in (a) and (b), respectively. Correspondingly, Figs. 13(d) and 13(e) show the PFM phase images of the domain stripes written by a negatively −150-V biased tip scanning in the direction antiparallel to the spontaneous polarization $\mathbf{P}_s$ measured with an on-shelf time gap of one year, and Fig. 13(f) shows the Fourier transform of the domain stripes, where the upper and the lower parts correspond to the cases for (d) and (e), respectively. The tip scanning speed in both cases is 80 μm/s. One sees that no noticeable degradation is observed.

[1] G. Poberaj, H. Hu, W. Sohler, and P. Gunter, Lithium niobate on insulator (LNOI) for micro-photonic devices, Laser Photonics Rev. **6,** 488 (2012).

[2] A. Boes, B. Corcoran, L. Chang, J. Bowers, and A. Mitchell, Status and potential of lithium niobate on insulator (LNOI) for photonic integrated circuits, Laser Photonics Rev. **12,** 1700256 (2018).

[3] A. Honardoost, K. Abdelsalam, and S. Fathpour, Rejuvenating a versatile photonic material: Thin-film lithium niobate, Laser Photonics Rev. **14,** 2000088 (2020).

[4] D. Zhu, L. Shao, M. Yu, R. Cheng, B. Desiatov, C. J. Xin, Y. Hu, J. Holzgrafe, S. Ghosh, A. Shams-Ansari, E. Puma, N. Sinclair, C. Reimer, M. Zhang, and M. Lončar, Integrated photonics on thin-film lithium niobate, Adv. Opt. Photonics **13,** 242 (2021).

[5] Y. Jia, L. Wang, and F. Chen, Ion-cut lithium niobate on insulator technology: Recent advances and perspectives, Appl. Phys. Rev. **8,** 011307 (2021).

[6] L. Hesselink, S. S. Orlov, A. Liu, A. Akella, D. Lande, and R. R. Reurgaonkar, Photorefractive materials for non-volatile volume holographic data storage, Science **282,** 1089 (1998).

[7] A. Q. Jiang, W. P. Geng, P. Lv, J. W. Hong, J. Jiang, C. Wang, X. J. Chai, J. W. Lian, Y. Zhang, R. Huang, D. W. Zhang, J. F. Scott, and C. S. Hwang, Ferroelectric domain wall memory with embedded selector realized in LiNbO$_3$ single crystals integrated on Si wafers, Nat. Mater. **19,** 1188 (2020).

[8] X. Chai, J. Jiang, Q. Zhang, X. Hou, F. Meng, J. Wang, L. Gu, D. W. Zhang, and A. Q. Jiang, Nonvolatile ferroelectric field-effect transistors, Nat. Commun. **11,** 2811 (2020).

[9] C. Wang, M. Zhang, X. Chen, M. Bertrand, A. Shams-Ansari, S. Chandrasekhar, P. Winzer, and M. Loncar, Integrated lithium niobate electro-optic modulators operating at CMOS-compatible voltages, Nature **562,** 101 (2018).

[10] M. He, M. Xu, Y. Ren, J. Jian, Z. Ruan, Y. Xu, S. Gao, S. Sun, X. Wen, L. Zhou, L. Liu, C. Guo, H. Chen, S. Yu, L. Liu, and X. Cai, High-performance hybrid silicon and lithium niobate mach-zehnder modulators for 100 Gbit/s and beyond, Nat. Photon. **13,** 359 (2019).

[11] M. Li, J. Ling, Y. He, U. A. Javid, S. Xue, and Q. Lin, Lithium niobate photonic-crystal electro-optic modulator, Nat. Commun. **11,** 4123 (2020).

[12] R. Wu, M. Wang, J. Xu, J. Qi, W. Chu, Z. Fang, J. Zhang, J. Zhou, L. Qiao, Z. Chai, J. Lin, and Y. Cheng, Long low-loss-litium niobate on insulator waveguides with sub-nanometer surface roughness, Nanomaterials (Basel) **8,** 910 (2018).

[13] M. Zhang, B. Buscaino, C. Wang, A. Shams-Ansari, C. Reimer, R. Zhu, J. M. Kahn, and M. Loncar, Broad-band electro-optic frequency comb generation in a lithium niobate microring resonator, Nature **568,** 373 (2019).

[14] J.-Y. Chen, Z.-H. Ma, Y. M. Sua, Z. Li, C. Tang, and Y.-P. Huang, Ultra-efficient frequency conversion in quasi-phase-matched lithium niobate microrings, Optica **6,** 1244 (2019).

[15] J. Zhao, C. Ma, M. Rusing, and S. Mookherjea, High Quality Entangled Photon Pair Generation in Periodically Poled Thin-Film Lithium Niobate Waveguides, Phys. Rev. Lett. **124,** 163603 (2020).

[16] S. Yuan, Y. Wu, Z. Dang, C. Zeng, X. Qi, G. Guo, X. Ren, and J. Xia, Strongly Enhanced Second Harmonic Generation in a Thin Film Lithium Niobate Heterostructure Cavity, Phys. Rev. Lett. **127,** 153901 (2021).

[17] Q. Luo, C. Yang, R. Zhang, Z. Hao, D. Zheng, H. Liu, X. Yu, F. Gao, F. Bo, Y. Kong, G. Zhang, and J. Xu, On-chip erbium-doped lithium niobate microring lasers, Opt. Lett. **46,** 3275 (2021).

[18] Z. Hao, L. Zhang, A. Gao, W. Mao, X. Lyu, X. Gao, F. Bo, F. Gao, G. Zhang, and J. Xu, Periodically poled lithium niobate whispering gallery mode microcavities on a chip, Sci. China-Phys. Mech. Astron. **61,** 114211 (2018).

[19] S. Zhu, Y. Zhu, and N. Ming, Quasi-phase-matched third-harmonic generation in a quasi-periodic optical superlattice, Science **278,** 843 (1997).

[20] A. Kuroda, S. Kurimura, and Y. Uesu, Domain inversion in ferroelectric MgO:LiNbO$_3$ by applying electric fields, Appl. Phys. Lett. **69,** 1565 (1996).

[21] K. Mizuuchi, A. Morikawa, T. Sugita, and K. Yamamoto, Electric-field poling in Mg-doped $LiNbO_3$, J. Appl. Phys. **96**, 6585 (2004).

[22] C. L. Sones, M. C. Wengler, C. E. Valdivia, S. Mailis, R. W. Eason, and K. Buse, Light-induced order-of-magnitude decrease in the electric field for domain nucleation in MgO-doped lithium niobate crystals, Appl. Phys. Lett. **86**, 212901 (2005).

[23] M. Fujimura, T. Sohmura, and T. Suhara, Fabrication of domain-inverted gratings in $MgO:LiNbO_3$ by applying voltage under ultraviolet irradiation through photomask at room temperature, Electron. Lett. **39**, 719 (2003).

[24] A. C. Muir, C. L. Sones, S. Mailis, R. Eason, T. Jungk, A. Hoffmann, and E. Soergel, Direct-writing of inverted domains in lithium niobate using a continuous wave ultraviolet laser, Opt. Express **16**, 2336 (2008).

[25] V. Y. Shur, D. S. Chezganov, M. M. Smirnov, D. O. Alikin, M. M. Neradovskiy, and D. K. Kuznetsov, Domain switching by electron beam irradiation of z^+-polar surface in Mg-doped lithium niobate, Appl. Phys. Lett. **105**, 052908 (2014).

[26] L. S. Kokhanchik and T. R. Volk, Domain inversion in $LiNbO_3$ and Zn-doped $LiNbO_3$ crystals by the electron-beam irradiation of the nonpolar *Y*-surface, Appl. Phys. B **110**, 367 (2012).

[27] O. Kolosov, A. Gruverman, J. Hatano, K. Takahashi, and H. Tokumoto, Nanoscale Visualization and Control of Ferroelectric Domains by Atomic Force Microscopy, Phys. Rev. Lett. **74**, 4309 (1995).

[28] M. Abplanalp, J. Fousek, and P. Gunter, Higher Order Ferroic Switching Induced by Scanning Force Microscopy, Phys. Rev. Lett. **86**, 5799 (2001).

[29] G. Rosenman, P. Urenski, A. Agronin, Y. Rosenwaks, and M. Molotskii, Submicron ferroelectric domain structures tailored by high-voltage scanning probe microscopy, Appl. Phys. Lett. **82**, 103 (2003).

[30] N. A. Pertsev and A. L. Kholkin, Subsurface nanodomains with in-plane polarization in uniaxial ferroelectrics via scanning force microscopy, Phys. Rev. B **88**, 174109 (2013).

[31] R. V. Gainutdinov, T. R. Volk, and H. H. Zhang, Domain formation and polarization reversal under atomic force microscopy-tip voltages in ion-sliced $LiNbO_3$ films on $SiO_2/LiNbO_3$ substrates, Appl. Phys. Lett. **107**, 162903 (2015).

[32] D. O. Alikin, A. V. Ievlev, A. P. Turygin, A. I. Lobov, S. V. Kalinin, and V. Y. Shur, Tip-induced domain growth on the non-polar cuts of lithium niobate single-crystals, Appl. Phys. Lett. **106**, 182902 (2015).

[33] A. Ievlev, D. Alikin, A. Morozovska, O. V. Varenyk, E. Eliseev, A. Kholkin, V. Shur, and S. Kalinin, Symmetry breaking and electrical frustration during tip-induced polarization switching in the nonpolar cut of lithium niobate single crystals, ACS Nano **91**, 769 (2015).

[34] A. Boes, V. Sivan, G. Ren, D. Yudistira, S. Mailis, E. Soergel, and A. Mitchell, Precise, reproducible nanodomain engineering in lithium niobate crystals, Appl. Phys. Lett. **107**, 022901 (2015).

[35] S. E. Harris, Proposed backward wave oscillation in the infrared, Appl. Phys. Lett. **9**, 114 (1966).

[36] C. Canalias and V. Pasiskevicius, Mirrorless optical parametric oscillator, Nat. Photon. **1**, 459 (2007).

[37] L. Gui, H. Hu, M. García-Granda, and W. J. O. e. Sohler, Local periodic poling of ridges and ridge waveguides on *x*- and *y*-cut $LiNbO_3$ and its application for second harmonic generation, Opt. Express **17**, 3923 (2009).

[38] P. Mackwitz, M. Rüsing, G. Berth, A. Widhalm, K. Müller, and A. Zrenner, Periodic domain inversion in *x*-cut single-crystal lithium niobate thin film, Appl. Phys. Lett. **108**, 152902 (2016).

[39] B. J. Stanicki, M. Younesi, F. J. F. Löchner, H. Thakur, W.-K. Chang, R. Geiss, F. Setzpfandt, Y.-H. Chen, and T. Pertsch, Surface domain engineering in lithium niobate, OSA Continuum **3**, 345 (2020).

[40] J. Zhao, M. Rüsing, M. Roeper, L. M. Eng, and S. Mookherjea, Poling thin-film *x*-cut lithium niobate for quasi-phase matching with sub-micrometer periodicity, J. Appl. Phys. **127**, 193104 (2020).

[41] M. Schröder, A. Haußmann, A. Thiessen, E. Soergel, T. Woike, and L. M. Eng, Conducting domain walls in lithium niobate single crystals, Adv. Funct. Mater. **22**, 3936 (2012).

[42] G. Catalan, J. Seidel, R. Ramesh, and J. F. Scott, Domain wall nanoelectronics, Rev. Mod. Phys. **84**, 119 (2012).

[43] E. A. Eliseev, A. N. Morozovska, G. S. Svechnikov, V. Gopalan, and V. Y. Shur, Static conductivity of charged domain walls in uniaxial ferroelectric semiconductors, Phys. Rev. B **83**, 235313 (2011).

[44] C. S. Werner, S. J. Herr, K. Buse, B. Sturman, E. Soergel, C. Razzaghi, and I. Breunig, Large and accessible conductivity of charged domain walls in lithium niobate, Sci. Rep. **7**, 9862 (2017).

[45] B. Kirbus, C. Godau, L. Wehmeier, H. Beccard, E. Beyreuther, A. Haußmann, and L. M. Eng, Real-time 3D imaging of nanoscale ferroelectric domain wall dynamics in lithium niobate single crystals under electric stimuli: Implications for domain-wall-based nanoelectronic devices, ACS Appl. Nano Mater. **2**, 5787 (2019).

[46] C. Godau, T. Kampfe, A. Thiessen, L. M. Eng, and A. Haussmann, Enhancing the domain wall conductivity in lithium niobate single crystals, ACS Nano **11**, 4816 (2017).

[47] A. A. Esin, A. R. Akhmatkhanov, and V. Y. Shur, Tilt control of the charged domain walls in lithium niobate, Appl. Phys. Lett. **114**, 092901 (2019).

[48] A. Labuda and R. Proksch, Quantitative measurements of electromechanical response with a combined optical beam and interferometric atomic force microscope, Appl. Phys. Lett. **106**, 253103 (2015).

[49] S. Hong, J. Woo, H. Shin, J. U. Jeon, Y. E. Pak, E. L. Colla, N. Setter, E. Kim, and K. No, Principle of ferroelectric domain imaging using atomic force microscope, J. Appl. Phys. **89**, 1377 (2001).

[50] B. D. Huey, C. Ramanujan, M. Bobji, J. Blendell, G. White, R. Szoszkiewicz, and A. Kulik, The importance of distributed loading and cantilever angle in piezo-force microscopy, J. Electroceram. **13**, 287 (2004).

[51] T. Cui, S. Mukherjee, P. M. Sudeep, G. Colas, F. Najafi, J. Tam, P. M. Ajayan, C. V. Singh, Y. Sun, and T. Filleter, Fatigue of graphene, Nat. Mater. **19**, 405 (2020).